



Error analysis of large-diameter subaperture stitching Fresnel diffractive elements

HAOLIN ZHANG,^{1,2,3,4} HUA LIU,^{1,*} WENBIN XU,⁴ ANGEL LIZANA,² XIAODUO WANG,⁵ AND ZHENWU LU⁴

¹Center for Advanced Optoelectronic Functional Materials Research, and Key Laboratory for UV-Emitting Materials and Technology of Ministry of Education, Northeast Normal University, 5268 Renmin Street, Changchun 130024, China

²Departamento de Física, Universitat Autònoma de Barcelona, Bellaterra 08193, Spain

³University of Chinese Academy of Sciences, Beijing 100039, China

⁴Changchun Institute of Optics, Fine Mechanics and Physics, Chinese Academy of Sciences, Changchun, Jilin 130033, China

⁵Shenyang Institute of Automation, Chinese Academy of Sciences, Shenyang 110016, China

*Corresponding author: liuhua_rain@aliyun.com

Received 5 May 2017; revised 2 August 2017; accepted 15 August 2017; posted 21 August 2017 (Doc. ID 295326); published 19 September 2017

Image quality is dramatically influenced by the stitching errors in a large-diameter stitching Fresnel lens. In this paper, we studied three kinds of errors that can cover all stitching errors in a Cornwell deployed Fresnel lens. In particular, a 300-mm-diameter, three-belt deployed Fresnel diffractive lens was simulated to investigate the stitching error. The star test and the resolution board test experiments were conducted, and the experimental results fit the simulation results. This means that our error analysis theory and simulation method are efficient and accurate and could be used to guide future super-large aperture stitching. © 2017 Optical Society of America

OCIS codes: (050.1380) Binary optics; (050.1220) Apertures; (110.3000) Image quality assessment.

<https://doi.org/10.1364/AO.56.007672>

1. INTRODUCTION

Interest in using large-aperture diffractive optical elements (DOEs) for fabrication of the primary lenses of space telescopes has largely been discussed in specialized literatures [1–6], and they present interesting benefits when compared with other alternatives. For instance, DOE-based primary lenses show loose surface shape tolerance and are lightweight. In 1999, Hyde first proposed the Eyeglass telescope system, which uses a large-diameter diffractive lens as the primary lens and a separate telescope as the mobile eyepiece [7]. Based on this sketch, Serre *et al.* designed a ground-based prototype and tested the telescope system. Although this new system was very promising, a drawback was the resulting system resolution, which was limited due to the small aperture of the primary lens, being only 8 cm [8]. In 2002, Hyde proposed the MOIRE system, which shares the same structure as the Eyeglass. From his studies, he demonstrated that it is very difficult to fabricate large-diameter DOEs directly, and the best way to fabricate them is to process small diffractive element sections and then properly stitch them together [9].

Under this scenario, the study of primary lenses based on stitched DOEs has become a matter of interest. Early *et al.* assembled a 5-m-diameter, 250-m focal length glass diffractive lens by using 72 rectangular and triangular panels [10]. Domber *et al.* assembled a 5-m-aperture, 45° segmented diffractive membrane that consists of three petals and six DOEs. They tested the

membrane, and the obtained results showed that the root mean square (RMS) wavefront error of a single DOE was 112 nm, and the quality of the obtained images in terms of the National Imagery Interpretability Rating Scale (NIIRS) reached values of 2.3 by using a LED source under laboratory conditions [11]. Although Domber *et al.* demonstrated the optical performance of the stitching membrane and highlighted the interest of using it for telescope fabrication, the study of the influence of the stitching error on the final image quality was not provided yet. However, in real implementations, these errors exist due to imprecise stitching. As a consequence, the final image quality is reduced to a certain extent. Yan *et al.* recently conducted the study of flat-stitching error of photon sieves. Their study focused only on a squared aperture, but no other type of aperture has been studied so far. Moreover, they studied only a one-dimensional stitching error, which could not fully cover five-dimensional in real stitching. More importantly, no quantitative stitching error formulas have been obtained [12].

The outline of this paper is as follows. First, in Section 2, we briefly review the design of the Cornwell layout, one of the most commonly implemented aperture layouts. Next, in Section 3, we provide the mathematical equations of the axis error, the radial error, and the rotation error of subaperture stitching DOEs. Those calculations are based on wave aberration theory and Rayleigh criteria. Afterwards, in Section 4, we perform MATLAB and Zemax co-simulation of a

300-mm-diameter, three-belt deployed Fresnel lens. In Section 5, the star test and the resolution board test of the lens are carried out; the experimental results fitted the simulation results. The conclusions are provided in Section 6.

2. SUBAPERTURE LAYOUT

Nowadays, the most commonly used subaperture layouts are the Cornwell layout, the Circle layout, and the Golay layout [13]. Among them, the most widely studied is the Cornwell layout. In this layout, all the apertures are evenly distributed within the same belt, and different belts are constructed by forming together different concentric rings of certain diameters. Shapes for the apertures to be applied have been proposed as circular, rectangular, and trapezoidal, each one finding its own application [14]. As an example, Fig. 1 shows a Cornwell deployed Fresnel lens with circle subapertures (yellow circles).

We first analyze the most densely distributed situation in a Cornwell deployed Fresnel lens. Namely, one subaperture in any belt is tangent to its adjacent subapertures in the neighboring belt. In addition, each subaperture is also tangent to its adjacent one in the same belt. In this arrangement, shown in Fig. 1, each belt has m subapertures, and the number of the belts is n .

As an example, let us analyze one particular subaperture labeled by the subscript i . To fully characterize this subaperture, we need to know its azimuthal angle $2\alpha_i$ (angular position of the subaperture into the belt), the half-width of the belt d_n , where the subaperture is placed, the radius of this subaperture r_n (all the subapertures in a particular belt share the same radius), and the length D from the middle of this belt to the point O (the center of the whole lens). We also label (x_i, y_i) as the central coordinates of the subaperture i , and d_{in} as the distance from O to the inner margin of the first belt. According to this geometric relation, we can derive that

$$d_n = \frac{\sin \alpha (d_{in} + 2d_1 + \dots + 2d_{n-1})}{1 - \sin \alpha} \quad n \geq 2. \tag{1}$$

Due to the fact that the subapertures are tangent among each other, the coordinates of the i subaperture are

$$x_i = \sin(\alpha_i)(d_{in} + 2d_1 + \dots + 2d_{n-1} + d_n) \quad n \geq 2, \tag{2}$$

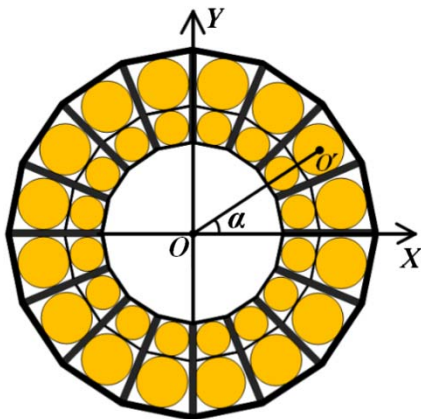


Fig. 1. Cornwell deployed Fresnel lens with circle subapertures.

$$y_i = \cos(\alpha_i)(d_{in} + 2d_1 + \dots + 2d_{n-1} + d_n) \quad n \geq 2. \tag{3}$$

Any distributed Cornwell Fresnel lens can be designed by considering these three equations. However, because mechanical calibration structures are needed to be installed among the adjacent apertures in some practical applications, these apertures are not generally tangent, and r_n should be smaller than d_n .

3. SUBAPERTURE STITCHING ERROR ANALYSIS

The surface of the Fresnel lens discussed in Section 2 can be regarded as flat if we do not consider errors caused by fabrication or by temperature variation. Under this circumstance, stitching errors are still introduced due to the deviations of the real subaperture positions from their corresponding ideal ones. These stitching errors may arise in three different forms: as offset errors in the radial direction, offset errors in the axial direction, and rotating errors around the radius. For the sake of clarity, these error sources are represented in Fig. 2.

The Fresnel lens in Fig. 2 contains six panels. All panels are ideally stitched with the exception of panel B. In particular, panel B contains radial and rotating errors. Thus, its real position does not coincide with the ideal one (the ideal position is presented in Fig. 2 by a gray circle). Therefore, these three types of error tolerances can be estimated by calculating optical path differences. Note that we can use this model to characterize the stitching error for any type of diffractive element. In the following, the above stated stitching errors are mathematically described.

A. Radial Offset Error Tolerance

Let the focal length of a given lens be f , the incident height of the edge ray r , and the offset in the radial direction Δr . When illuminating the system with a collimated beam, the optical path difference between the ideal and the real ray trajectories ΔL_{radius} can be written as

$$\Delta L_{\text{Radius}} = \frac{r}{f} \Delta r. \tag{4}$$

According to Rayleigh Criteria, the peak-to-valley (PV) wavefront error of a precise optical system should be less than $\lambda/10$, and, thus, the corresponding radial offset error tolerance must accomplish

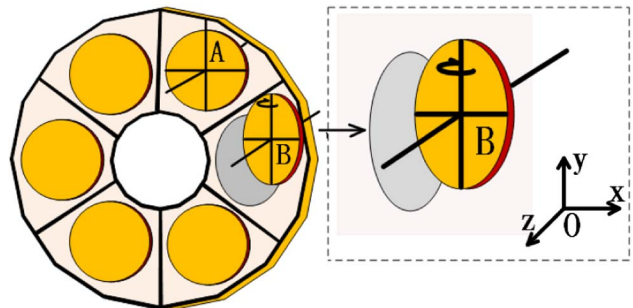


Fig. 2. Six-subaperture deployed Fresnel lens.

$$\Delta r = \frac{\lambda f^{\#}}{5}. \quad (5)$$

B. Axial Offset Error Tolerance

Under the same scenario in case *a*, but for an offset in the axial direction Δz , the optical path difference ΔL_{radius} is written as

$$\Delta L_{\text{Axis}} = \frac{r^2}{2f^2} \Delta z, \quad (6)$$

and the axial error tolerance must accomplish

$$\Delta z = \frac{4\lambda f^{\#2}}{5}. \quad (7)$$

C. Rotating Error Tolerance

Figure 3 illustrates the rotating error scheme. The edge of the aperture deviates from its ideal position A to the real one B due to the rotating error, where the rotating angle is θ . In the case of an aperture without rotating error, L_3 represents the optical path from A to the focal point F. By contrast, when the rotating error translates the aperture edge from point A to point B, L_2 provides the optical path from point B to F. Spot C can be determined by finding the intersection point between the horizontal line passing through point A and the prolongation of the aperture in the rotating direction (dashed line in Fig. 3); L_1 provides the optical path from point C to F. We label Δz as the axial distance from A to B, and $\Delta z'$ the axial distance from B to C.

By considering the rotating error, the optical path difference ΔL_{Rotate} before and after applying the rotation θ can be described as

$$\Delta L_{\text{Rotate}} = L_2 + \Delta z - L_3. \quad (8)$$

By applying L_1 to the equation, Eq. (8) can be written as

$$\Delta L_{\text{Rotate}} = (\Delta z + L_1 - L_3) + (L_2 - L_1). \quad (9)$$

Since values of $\Delta z'$ are much smaller than other distances in Fig. 3, they can be neglected. In such a case, the two terms in Eq. (9) represent the radial offset error and axial offset error, respectively. So,

$$\Delta L_{\text{Rotate}} = \frac{r^2}{2f^2} \Delta z + r \frac{\Delta r}{f}, \quad (10)$$

$$\Delta L_{\text{Rotate}} = \frac{r^3}{2f^2} \sin \theta + \frac{r^2}{f} (1 - \cos \theta), \quad (11)$$

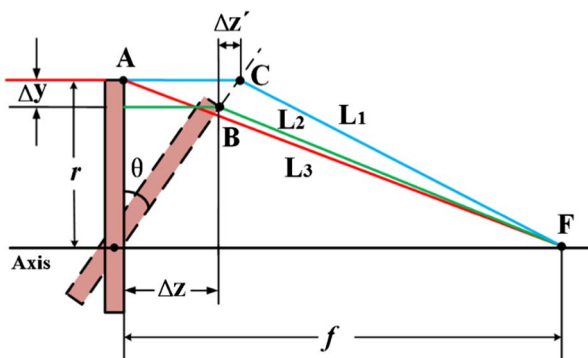


Fig. 3. Rotating error pattern.

$$\Delta L_{\text{Rotate}} = \frac{r \Delta \theta}{8(f^{\#})^2} \sin \theta + \frac{r(\Delta \theta)^2}{4f^{\#}}, \quad (12)$$

$$\Delta \theta = \frac{\sqrt{6.4\lambda(f^{\#})^3 + r} - \sqrt{r}}{4f^{\#}\sqrt{r}}. \quad (13)$$

The rotating error described by Eq. (13) is relative to the center of a given subaperture, but not to the center of the whole diffractive lens. Moreover, the center of the subaperture does not generally coincide with the center of the lens. Hence, it is more accurate to study the error by using as criteria the whole lens center. Figure 4 sketches the error pattern relative to the lens center.

Note that O' is the center of a subaperture, the distance AB is its diameter, O is the center of the whole lens, and d is the length from O to O' . Then, $\Delta \theta'$ can be written as

$$\Delta \theta' = \arctan\left(\frac{r \sin(\Delta \theta)}{r \cos(\Delta \theta) + d}\right). \quad (14)$$

D. Comprehensive Error

Note that Eqs. (5), (7), and (14) represent the radial, the axial, and the rotating error tolerances, respectively. We can tell that the offset errors are proportional to $f^{\#}$; the rotating error is not only related to $f^{\#}$, but also related to its diameter and d .

In a real stitching process, these three above-stated errors appear at the same time, and they appear in 5 deg of freedom (DOF). If we use ΔL_i to represent the effect of individual errors on the wavefront distribution, and use W_i to represent the weight of each error (W_1 and W_2 for rotating errors in x and y directions, W_3 for the axial offset error, and W_4 and W_5 for radial offset errors in x and y directions), we have the following equation [Eq. (15)], and it can be used to estimate the total error tolerance of the stitching system:

$$\Delta L = \sqrt{W_1^2 \Delta L_1^2 + W_2^2 \Delta L_2^2 + W_3^2 \Delta L_3^2 + W_4^2 \Delta L_4^2 + W_5^2 \Delta L_5^2}. \quad (15)$$

According to Eq. (15), a certain error can be relaxed by properly assigning the weight of other error sources. What is more, once the real wavefront distribution is obtained, we can find out which subapertures have the stitching error. Moreover, we can also estimate the error type from the shape of the wavefront, which can be measured by using interferometric

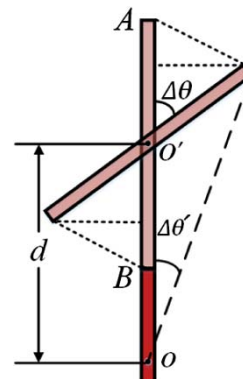


Fig. 4. Error pattern relative to the lens center.

techniques. Last but not least, the error values of the stitching lens can be calculated from the PV value of the wavefront.

4. SIMULATION METHOD OF SUBAPERTURE DOES

The simulation method used to describe a subaperture DOE stitching error is explained as follows. First, the phase distribution of a DOE is calculated, and the obtained information is loaded to the incident wavefront. Afterwards, the corresponding phase distribution in the focal plane is analyzed.

Let us start by studying the relation of an infinitesimal point of the ideally stitched subaperture, spatially described by the point (x_0, y_0, z_0) , and the corresponding point (x, y, z) affected by the stitching error. The two points can be related by the following linear system in the matrix form:

$$\begin{pmatrix} x \\ y \\ z \\ 1 \end{pmatrix} = A \cdot R \cdot B \cdot \begin{pmatrix} x_0 \\ y_0 \\ z_0 \\ 1 \end{pmatrix}, \quad (16)$$

where the matrices A , R , and B are written as follows:

$$A = \begin{pmatrix} 1 & 0 & 0 & 0 \\ 0 & 1 & 0 & 0 \\ 0 & 0 & 1 & 0 \\ t_x & t_y & t_z & 1 \end{pmatrix}, \quad R = \begin{pmatrix} 1 & 0 & 0 & 0 \\ 0 & \cos \alpha & \sin \alpha & 0 \\ 0 & -\sin \alpha & \cos \alpha & 0 \\ 0 & 0 & 0 & 1 \end{pmatrix},$$

$$B = \begin{pmatrix} \cos \beta & 0 & -\sin \beta & 0 \\ 0 & 1 & 0 & 0 \\ \sin \beta & 0 & \cos \beta & 0 \\ 0 & 0 & 0 & 1 \end{pmatrix}.$$

The first matrix A represents the offset error, t_x, t_y are the radial offset errors, and t_z is the axial offset error. Matrix R represents the axial rotating error for a rotation angle α , and matrix B is the radial rotating error (rotating angle as β). Then, the phase distribution of this point is

$$\phi(x, y, z) = -\frac{k}{2(f-z)}(x^2 + y^2). \quad (17)$$

Note that Eq. (17) provides the phase distribution of a single subaperture point affected by stitching errors, with k being the wavenumber ($k = 2\pi/\lambda$), and f the focal length of the lens. The overall phase distribution of the diffractive lens is the addition of the phase distributions of all the points, which can be described as

$$\phi_{\text{sum}}(x, y, z) = \sum_{i=0}^N \phi_i(x_i, y_i, z_i). \quad (18)$$

We want to emphasize that N in Eq. (18) represents the number of discrete points.

Once the total phase distribution is calculated, a “.DAT” file, which contains all phase values, is created by MATLAB. Then, we can simulate the lens in Zemax by using “Grid Phase” to describe the phase [15].

We want to note that during the radial offset error simulation, if the theoretical wavefront PV is $\lambda/10$, the PV in the Zemax should be $\lambda/5$. This is because in Zemax processing, all PV values of the wavefront are expressed in negative values. However, in our method, the radial offset makes the differences of phase values between a real wavefront and an ideal one to be both negative and positive, and the opposite.

5. EXPERIMENTAL TEST OF A 300-MM-DIAMETER STITCHING FRESNEL LENS

A. Design of the Diffractive Element

We designed a 300-mm-diameter amplitude Fresnel lens with a working wavelength of 632.8 nm and a focal length of 30,000 mm. For this focal length and diameter, the ring number s equation can be written as

$$s^2 \lambda^2 + 2s \lambda f = r_s^2. \quad (19)$$

Moreover, the corresponding widths are

$$w_s = \frac{f \lambda}{2r_s}. \quad (20)$$

After the calculation, this Fresnel element contains 592 rings, and the width of the outermost ring is 63.28 μm .

In this Fresnel lens, any amount of circular subapertures can be distributed. Here we evenly deployed the subapertures in three belts in order to facilitate the subsequent simulation. The width of the belts is the same as the diameters of their corresponding circular subapertures. The configuration of the lens is as follows: First, only one subaperture is deployed in A belt (see Fig. 5), and the center of this belt coincides with the center of the Fresnel lens ($D_1 = 0$ mm, $r_1 = 39.96$ mm). B belt is evenly distributing eight subapertures ($D_2 = 74.41$ mm, $r_2 = 14.35$ mm). The angle between the first subaperture and the x axis is 30° , and the angle between each two adjacent subapertures is 45° . In the case of C belt [see Fig. (5)], 12 subapertures are evenly distributed ($D_3 = 131.05$ mm, $r_3 = 18.94$ mm). The angle between the first subaperture in C belt and the x axis is 15° , and the angle between each two adjacent subapertures is 30° .

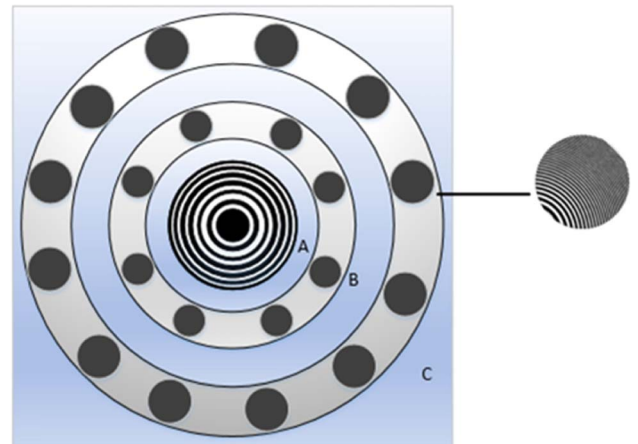


Fig. 5. 300-mm diameter, three-belt-distributed subaperture Fresnel lens.

The diameter of all subapertures in a particular belt is fixed to a value equal to the width of the belt where they are placed. The modulation of the wavefront of one subaperture in each belt is independent of that of the other subapertures in the same belt. The modulation result of the wavefront depends on the one subaperture that has the maximum error.

The PV of the Fresnel lens in Fig. 5 is 0.0048λ , and its Airy disk diameter is 0.154 mm. When the outer three subapertures in the first quadrant all move along the axis for 5.06 mm in the same direction, the PV is 0.1069λ . The wavefront maps are shown in Fig. 6.

We want to emphasize that for the sake of visualization, the wavefronts shown in Figs. 6(a) and 6(b) are re-scaled. To note the differences in the corresponding wavefront peak values, we added numerical scale bars in red (i.e., 0.0048λ and 0.1069λ , respectively).

Note that the excessive circular subapertures not only introduce difficulties in Fresnel lens fabrication, but also in the calibration. However, we know that the maximum error determines the wavefront of a whole belt. Thus, if a certain subaperture in a belt has the same error as the one in the belt, and the errors of other subapertures in such a belt are smaller, the modulation result of the wavefront for these circular subapertures is the same as the one shown by this single belt. Considering this, all the subapertures in a belt can be regarded as a whole, namely, a belt subaperture. More importantly, the error of this belt is the same as the maximum subaperture error.

By taking this into account, we designed the stitching Fresnel lens with belts instead of an array of tangential circles. The implemented configuration is as follows: The radius of A belt is 39.96 mm; the inner radius of B belt is 60.06 mm, and its outer radius is 88.76 mm; and finally, the inner radius of C belt is 112.11 mm, and its outer radius is 149.99 mm. A picture of the corresponding diffractive elements is shown in Fig. 7.

By simulating the scheme in Fig. 7, the corresponding Airy disk diameter is 0.153 mm, and the PV is 0.0049λ when all belts are ideally stitched. When C belt has a 5.06 mm axial offset error, the PV is 0.1029λ . The simulation results are shown in Fig. 8.

Note that by taking into account the values for the red scale bars in Figs. 6 and 8, we see how wavefronts share the same contour in the real implementation.

The wavefront PV values of the Fig. 5 pattern and Fig. 7 pattern are equivalent, considering the simulation results in Figs. 6 and 8. This demonstrates that the belt-distributed stitching Fresnel lens we proposed and the circular subapertures-based lens lead to the same modulation results on the wavefront. Hence, we want to note that it is feasible to use belt subapertures to replace circular ones. So, in order to simplify

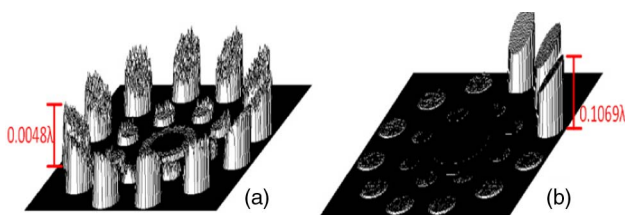


Fig. 6. Wavefront patterns: (a) ideal, (b) axial error is 5.06 mm.

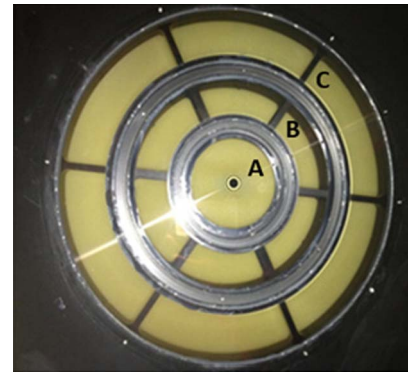


Fig. 7. 300-mm-diameter Fresnel lens.

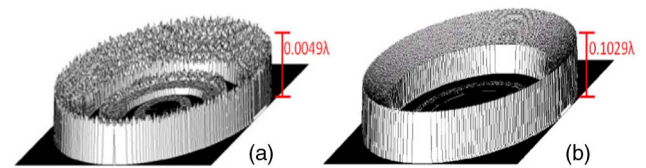


Fig. 8. Wavefront distributions: (a) ideal, (b) C-belt axial error is 5.06 mm.

the experiment, we used the three-belt-distributed model to make the analysis.

Then the theoretical error tolerances are calculated by the three equations in Section 2. The results are given in Table 1.

For larger quantitative information of the three-belt-based Fresnel lens, Figs. 9 and 10 show the modulation transfer functions (MTFs) of both the ideally stitched Fresnel lens (Fig. 9) and the lens with the C belt presenting a 5.06-mm axial offset error (Fig. 10), as a function of the spatial frequency.

The obtained simulated results show that: (i) the maximum signal frequency is 3.84 lp/mm when the modulation value is 0.1 if there is no stitching error; (ii) the maximum signal frequency decreases to 3.61 lp/mm when there exists a 5.06-mm axial error in the C belt.

Table 1. Theoretical Error Tolerances^a

	Radial Offset	Axial Offset	Rotation
A belt	47.83 μm	72.29 mm	2.77°
B belt	21.39 μm	14.46 mm	0.17°
C belt	12.66 μm	5.06 mm	0.08°

^aIn addition, the simulation results for C belt are given in Table 2.

Table 2. Simulation Results of C Belt^a

Error Type	Radial Offset	Axial Offset	Rotation
Error	12.66 μm	5.06 mm	0.08°
WF PV	0.1945 λ	0.1035 λ	0.978 λ
WF RMS	0.0494 λ	0.0399 λ	0.0229 λ

^aNote that the simulation results in Table 2 fit the theoretical calculation provided in Table 1.

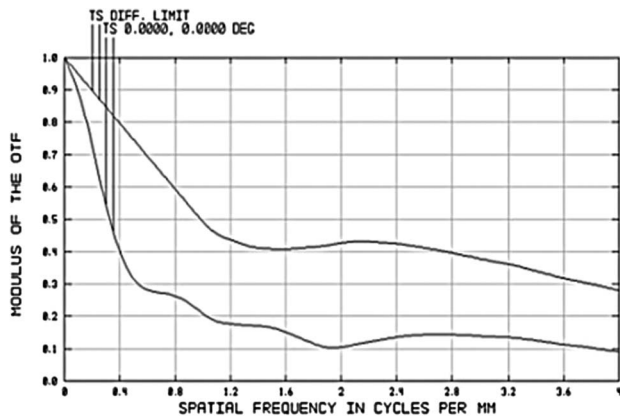


Fig. 9. MTF of the ideally stitched Fresnel lens.

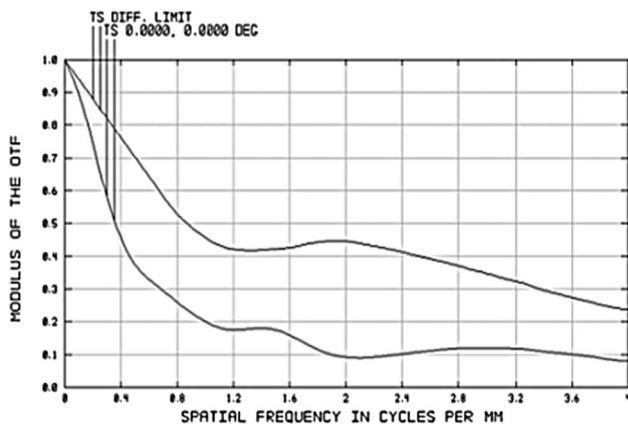


Fig. 10. MTF of the lens with C belt has a 5.06-mm axial offset error.

We also performed the simulation of the comprehensive error explained in Section 3 (d). We set the rotating error weight of $W_1 = W_2 = 0.67$, axial offset error weight of $W_3 = 0.67$, and the radial offset error weight of $W_4 = W_5 = 0.60$. Under these conditions, the wavefront PV is 0.2009λ , and the RMS is 0.0464λ at 0° field of view. The result shows that the sensitivities of both the rotating error and the radial offset error are higher than those of the axial offset error.

B. Imaging Test

Finally, we carried out the star test and the resolution board test of this three-belt-distributed subaperture Fresnel lens separately in order to verify our theoretical error analysis and the simulation process.

When performing the star test, we used a He–Ne laser (632.8 nm) to illuminate the Fresnel lens. A small pinhole with a diameter of $5\ \mu\text{m}$ was used to generate a collimated light beam. This collimated beam illuminated the Fresnel lens (Fig. 7) and thus focused to the focal panel. We first tested the star image of the lens with no stitching error. After this, the star image was tested again, but now we mechanically moved the C belt along the axial direction a distance of

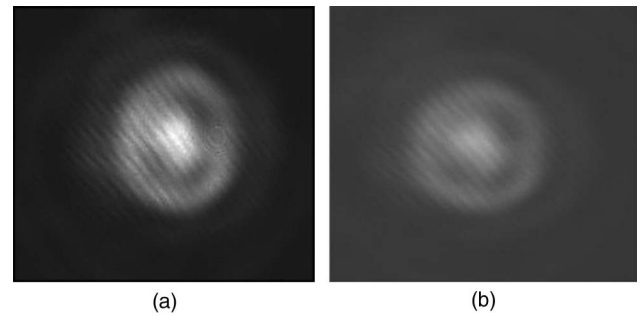


Fig. 11. Star test images: (a) ideal, (b) C-belt axial error is 6 mm.

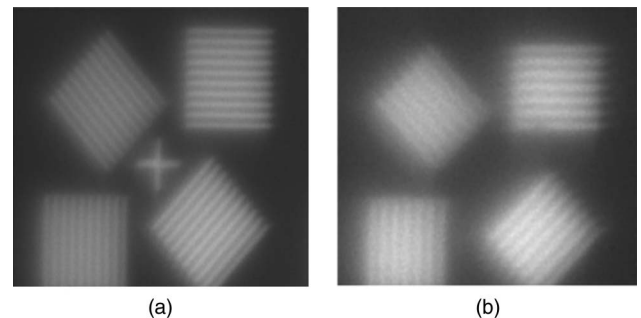


Fig. 12. Resolution board test: (a) ideal, (b) C-belt axial error is 6 mm.

6 mm to analyze the effect of an axial error. The obtained experimental results are provided, respectively, in Fig. 11.

Afterwards, we performed the resolution board test. In this case, the wavelength of the LED source ranged from 620 nm to 640 nm. In addition, the resolution board used included spatial frequencies ranging from 25 lp/mm to 100 lp/mm. The testing results obtained from the ideal and the C-belt axial error cases are, respectively, provided in Figs. 12(a) and 12(b).

Results given in Fig. 11 show that ideally stitched lenses are able to provide better images than those presenting stitching errors. The testing results in Fig. 12 indicate that the maximum signal frequency for an ideally stitched lens is 3.79 lp/mm, but when an axial error of 5.06 mm is set for the C belt, this maximum signal frequency reduces to 3.57 lp/mm. We want to emphasize that the testing results fit the simulation results.

6. CONCLUSION

In this paper, five degrees of freedom stitching errors, occurring during the fabrication of diffractive Fresnel lenses to be used as primary lenses of space telescopes, are described for the first time. The offset error tolerance and the rotating error tolerance were deduced by using Cornwell deployed diffractive elements that consist of circular subapertures. Moreover, we theoretically demonstrated the suitability of using belt-distributed apertures instead of arrays of circular subapertures, as they provide similar performance but the first arrangement is easier to implement in fabrication processes. Based on this latter result, we simulated a three-belt distribution of a 300-mm-diameter Fresnel lens. The simulation results showed that subapertures with a small

diameter and large $f^\#$ are preferable because they present larger error tolerances. Finally, the proposed Fresnel lens scheme (three-belt distribution) was experimentally tested by using the star and the resolution board tests for a 300-mm-diameter Fresnel lens. The experimental results show that the maximum signal frequency is 3.79 lp/mm for an ideally stitched system, and the maximum signal frequency decreases to 3.57 lp/mm if C belt has a 6-mm axial offset error. The experimental results fit the simulation results. Therefore, this work provides a theoretical framework suitable to study stitching errors in DOE and can be used to study future super-large diameter subaperture stitching diffractive elements.

Funding. People's Government of Jilin Province (20160519021JH); State Key Laboratory of Luminescence and Applications.

REFERENCES

1. R. Hyde, *Eyeglass Large Aperture, Lightweight Space Optics FY2000–FY2002 LDRD Straight Initiative* (US Department of Energy, 2003).
2. I. M. Barton, J. A. Britten, S. N. Dixit, L. J. Summers, I. M. Thomas, M. C. Rushford, K. Lu, R. A. Hyde, and M. D. Perry, "Fabrication of large-aperture lightweight diffractive lenses for use in space," *Appl. Opt.* **40**, 447–451 (2001).
3. M. Gruneisen, R. Dymale, J. Rotge, L. Desandre, and D. Lubin, "Compensated telescope system with programmable diffractive optic," *Opt. Eng.* **44**, 023201 (2004).
4. D. Buralli and M. Morris, "Design of two-and three element diffractive Keplerian telescopes," *Appl. Opt.* **31**, 38–43 (1992).
5. G. Andersen and D. Tullson, "Photon sieve telescope," *Proc. SPIE* **6265**, 626523 (2006).
6. G. Andersen and D. Tullson, "Broadband antihole photon sieve telescope," *Appl. Opt.* **46**, 3706–3708 (2007).
7. R. Hyde, "Eyeglass. 1. Very large aperture diffractive telescope," *Appl. Opt.* **38**, 4198–4212 (1999).
8. D. Serre, P. Deba, and L. Koechlin, "Fresnel interferometric imager: ground-based," *Appl. Opt.* **48**, 2811–2820 (2009).
9. R. Hyde, S. Dixit, A. Weisberg, and M. Rushford, "Eyeglass, a very large aperture diffractive space telescope," *Proc. SPIE* **4849**, 28–39 (2002).
10. J. Early, R. Hyde, and R. Baron, "Twenty meter space telescope based on diffractive Fresnel lens," *Proc. SPIE* **5166**, 148–156 (2004).
11. J. L. Domber, P. Atcheson, and J. Kommers, "MOIRE: ground test bed results for a large membrane telescope," in *Space Structures Conference* (2014), 2014-1510.
12. G. Jin, J. Yan, H. Liu, X. Zhong, and Y. Yan, "Flat-stitching error analysis of large-aperture photon sieves," *Appl. Opt.* **53**, 90–95 (2014).
13. J. Pitman, A. Duncan, D. Stubbs, R. Sigler, R. Kendrick, E. Smith, J. Mason, G. Delory, J. H. Lipps, M. Manga, J. Graham, I. de Pater, S. Reiboldt, E. Bierhaus, J. B. Dalton, J. Fienup, and J. Yu, "Remote sensing space science enabled by the multiple instrument distributed aperture sensor (MIDAS) concept," *Proc. SPIE* **5555**, 301–310 (2004).
14. W. D. Tandy, P. Atcheson, J. Domber, and A. Seltzer, "MOIRE gossamer space telescope-structural challenges and solutions," in *53rd AIAA/ASME/ASCE/AHS/ASC Structures, Structural Dynamics and Materials Conference* (2012), 2012-1670.
15. Zemax Development Corporation, "User's Guide," www.zemax.com.